Understanding pulsed jet impingement cooling by instantaneous heat flux matching at solid-liquid interfaces

Khan Md. Rabbi, Jake Carter, and Shawn A. Putnam*
Department of Mechanical and Aerospace Engineering, University of Central Florida, Orlando, Florida 32816, USA

(Received 7 October 2019; accepted 19 August 2020; published 11 September 2020)

In recent decades, jet impingement cooling has gained significant attention due to its ability to remove large thermal loads from local heating zones. This study demonstrates the performance of pulsed jet impingement cooling on a Ti-coated glass window. Infrared (IR) thermography data are analyzed to generate heat transfer coefficient (HTC) maps for a range of heat fluxes ($q'' \approx$ 20–60 W/cm^2) and jet pulsation frequencies ($f_p \approx$ 7–25 Hz). Heat transfer coefficients are observed to scale as $h \propto \sqrt{2f_p}$ with local maximum values at the center of the jet stagnation zone. For reference, $h^{\max} \approx$ 15 kW/m^{2}K is found for $q'' \approx$ 60 W/cm^2 and $f_p \approx$ 25 Hz. Moreover, a jet pulsation frequency of $f_p \approx$ 15 Hz matches well with both the bubble release rate and dry-out occurrence rate within 50 and 80 ms, respectively, at $q'' =$ 60 W/cm^2. At heat fluxes >40 W/cm^2, boiling regimes were captured in terms of cyclic events of bubble growth, bubble collapse, dry-out, partial rewetting, and full rewetting. Finally, a theoretical model is proposed based on both the HTC expected for a steady jet and HTC augmentation due instantaneous heat flux matching for a pulsed jet at the jet-wall interface. The correlation between experiments and theory are reasonable, yet there are still unresolved complexities associated with thermofluid instabilities, decoupling the transient latent heat and sensible heat transfer mechanisms, and first-principles modeling of the spatiotemporal surface temperature and flow-field oscillations induced by a pulsed jet.

DOI: 10.1103/PhysRevFluids.5.094003

I. INTRODUCTION

Innovations in thermal management for current and future mechanical, optical, and microelectronic devices is getting extremely challenging. This is in large part a side product of the demand for efficient, high-power density devices, e.g., such tiny, powerful gadgets challenge not only on our theoretical understandings of local and highly transient heat and mass transfer but also the conceptual design and practical implementation of a new cooling configuration.

Currently there are many different cooling technologies to manage this high-power density problem. Among them, pool boiling, microchannel flow boiling, spray cooling, and jet impingement cooling provide the best cooling performance metrics for high heat-density applications [1–5]. With this said, how do you get the cooling fluid in and out of nano- or microchannels with appreciable mass fluxes? Nevertheless, among these cooling techniques, jet impingement cooling shows the best performance for cooling local hot spots in terms of its correspondingly high heat transfer coefficient, surface temperature control, directional fluid flow fields, and capability for cooling with reduced liquid coolant inventories [6,7]. However, jet impingement cooling with steady and free-stream jets has several thermophysical limits for optimal heat transfer at the solid-liquid interface. For example,

*shawn.putnam@ucf.edu

at high mass flow rates, liquid flooding effects can lead to cooling instabilities and reductions in the liquid-to-vapor (phase-change) cooling efficiency, which effectively cap the overall heat transfer coefficient to lower limit values. Likewise, jet impingement cooling at lower mass flow rates can also result in heat transfer coefficient reductions due to wall dry-out (and/or critical heat flux conditions). Therefore, an intermediate and tunable flow-field regime is desired to both avoid such instabilities and enhance the overall coefficient of performance (COP) of the thermal management system. Ideally, pulsed jets with tunable flow fields are desired, facilitating real-time thermal management control at the optimal length scales and timescales for high heat flux removal.

In recent years, many thermal engineers and scientists have been interested in the unsteady thermophysical behavior of pulsating jets. Much of this work has been inspired by the pioneering research of Nevins and Ball [8]. For instance, Hofmann *et al.* [9] studied pulsed jet cooling for different heating and flow-field conditions. For small nozzle-to-surface distance ($H/d \approx 2$), they observed that heat transfer increased if the jet pulsation frequency was high ($f_p > 175$ Hz) and on the same order of turbulence timescales. Moreover, using synthetic single-phase jets, Chaudhari *et al.* [10] observed 180% heat transfer enhancement by increasing the Reynolds number (Re) from 1150 to 4180. More recently, Lyu *et al.* [11] studied pulsed jets on semicircular heated surfaces with pulsation frequencies and nozzle-to-surface distance ratios ranging from $0 \text{ Hz} < f_p < 25$ Hz and $1 < H/d < 8$, respectively. They observed that pulsed jets outperformed steady jets for $H/d > 6$. Zargarabadi *et al.* [12] numerically investigated sinusoidally pulsed jets at pulsation frequencies of 40–160 Hz finding 2–8% enhancements in the Nusselt number (Nu). Moreover, Ghadi *et al.* [13] experimentally measured the effects of a pulsed turbulent jet. They observed that the jet pulsation frequency had significant influence on both the size and the formation process of the turbulent vortex structures. Therein the size and number of these vortices in the shearing layer were the key contributors to the wall heat transfer rate.

Despite the many recent advancements in pulsed jet cooling [12,14–21], to our knowledge, so far no theoretical progress has been made for predicting the heat transfer coefficient in terms of the jet pulsation frequency. This paper reports a simple theoretical model based on instantaneous heat flux matching at the solid-liquid interface. Correspondingly, a coupled Kapitza and Rayleigh-Taylor instability prediction is used to estimate the optimum pulsation frequency of the jet. These findings are based on transient thermal mapping and flow-field visualization experiments using infrared (IR) thermography and high-speed visible videography, respectively. Bubble growth, bubble collapse, dry-out zone formation, and rewetting events during the jet impingement boiling process are discussed in terms of the corresponding length scales and timescales of the pulsed jet cooling process. Finally, a validation effort between our experimental results and analytic predictions is made for subsequent predictions of the maximum heat transfer performance.

II. EXPERIMENTAL SETUP

A. Jet impingement flow loop

Figure 1 shows the pulsed jet cooling apparatus used for this work. A continuous, steady jet is generated by a two-phase flow pump developed by RINI technologies [22]. A stainless-steel syringe needle ($D_{\text{jet}} = 406\ \mu$m) is used to generate the steady jet stream. This steady jet is then mechanically chopped with a rotating filter wheel, facilitating jet pulsation frequencies and jet duty cycles ranging from 3–410 Hz and 20–100%, respectively (see the Supplementary Material [23] for the details). The spray or jet chamber houses an adjustable sample holder for electrical connections, sealing, and flow-loop connectors. The jet chamber can be moved relative to the jet nozzle and chopper wheel assembly to adjust both jet impingement point and the relative distance between jet source and the heated sample surface (e.g., H). This study focused on small-diameter, low-frequency pulsed jets (7–25 Hz) at 50% duty cycle and mass flux of $G = 795\ \text{kg/m}^2\text{s}$, corresponding to $H/D \approx 195$, $\text{Re} \approx 970$, and $\text{St} \approx 0.003$.

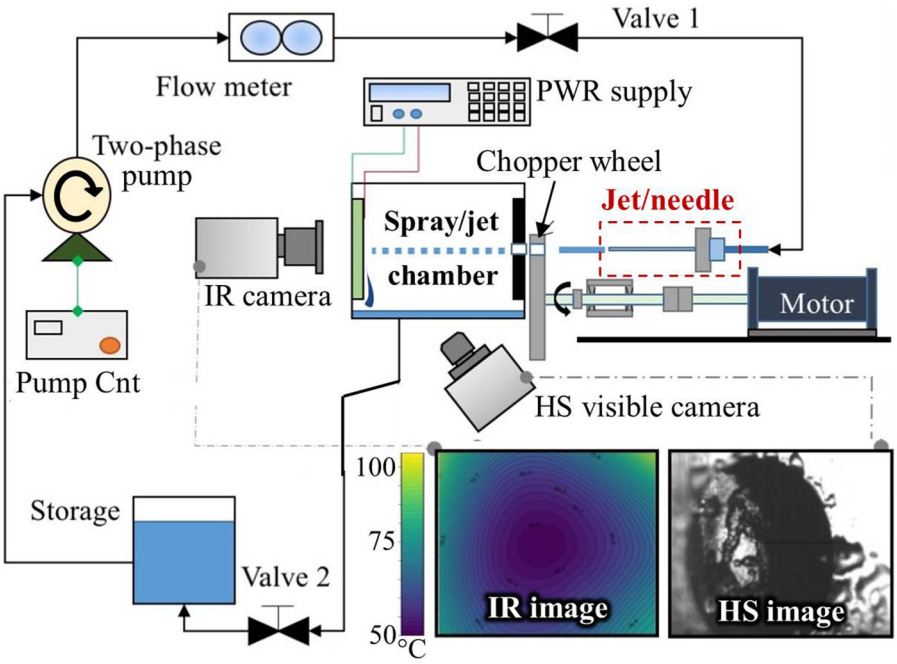

FIG. 1. Schematic diagram of the apparatus and flow-loop for pulsed jet impingement studies.

B. Heater fabrication

Figure 2 illustrates the heater or thermometer fabrication process. The titanium (Ti) thin film (50-Ω sheet resistance) was deposited on a fused silica (FS) glass substrate by dc magnetron sputtering. To maximize the adhesion of the Ti heater or thermometer to the glass substrate we first presputtered 10 nm of Ti on the glass substrate. Then we heat-treated this Ti-coated glass substrate on a hot plate in air at 400 °C for 2–3 min, followed by a rapid thermal quenching to room temperature on a Cu cold plate. This process facilitates a durable and strong bond Ti-glass bond. Then a polyamide mask was applied [Fig. 2(b)], facilitating Ti deposition onto only a selected portion of the glass substrate for a "band-aid"–shaped heater or thermometer geometry. Then the primary Ti (heater or thermometer) deposition was conducted for 20 min at constant power (33 W) in argon (8.3 mTorr pressure). The corresponding Ti deposition rate is 2 nm/min and the base pressure prior to deposition was 4×10^{-9} Torr (see the Supplemental Material [23] for the details).

To create the heater or thermometer busbars, Au was deposited at a deposition rate of 1.5 nm/min for 30 min at 33 W and 8.3 mTorr Ar. Electrically conductive silver paste (electrical resistivity, $\sigma = 0.0004$ Ω-cm) is applied on the Au busbars. In addition, a Cu foil wrapping is used for durable and improved electrical connections. Finally, the heater [Fig. 2(h)] is mounted in a Teflon-made sample stage holder with a machined stainless steel (SS) viewport cover. The SS cover has an O-ring groove outside the viewport area, where this whole assembly uses viton O-rings to prevent leaks and electrical shorting. A thin polyamide mask layer is also used on the top edges of Ti heater or thermometer surface (i.e., the region of O-ring contact) for extra mechanical protection from the o-ring seal during the required temperature cycling and pulsed jet cooling studies. The Ti heater was ohmically heated using an ac-dc power supply (Agilent HP 6813A, 300 Vrms, 1.75 kW). Four spring-loaded gold pins (mounted in the Teflon sample holder) provide electrical connections between the power supply and the thin-film heater assembly.

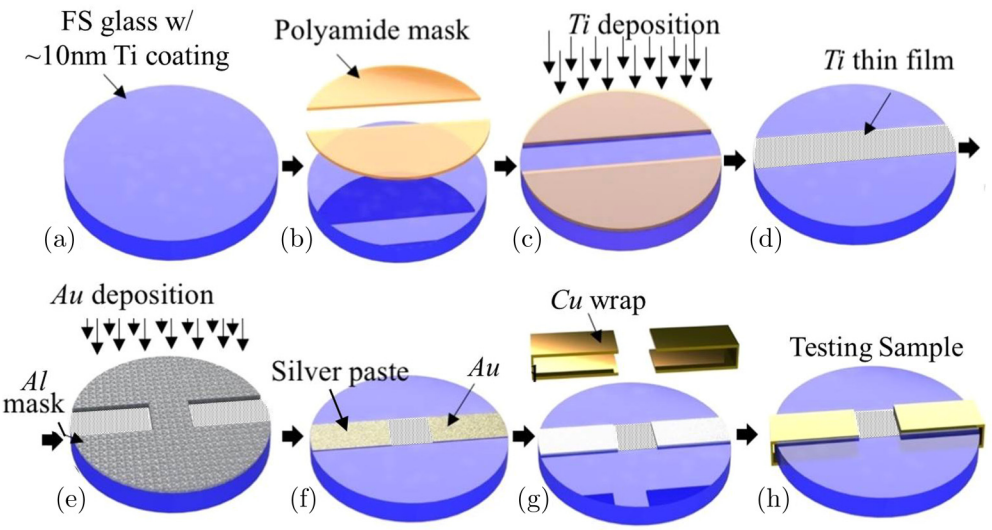

FIG. 2. Fabrication steps for the 1 cm × 1 cm Ti thin-film heater or thermometer. (a) Ultrasonically cleaned substrate with presputtered, heat-treated Ti/TiO_2 adhesion coating (≈10 nm). (b) Polyamide mask application. (c) Primary Ti thin-film deposition (≈100 nm). (d) Polyamide mask removal. (e) The Al mask application for subsequent Au deposition ("band-aid" Ti heater or thermometer). (f) Electrically conductive Ag paste application on Au busbars. (g) Application of Cu foil or busbar wraps. (h) Final heater configuration for loading into spray or jet chamber.

C. Visible imaging and temperature mapping

To visualize the fluid flow-field and map the surface temperature on the heater surface, we used both a high-speed visible camera (Phantom V12.1, 640 × 480 pixels, resolution = 44 μm/pixel) and FLIR IR thermal camera (FLIR SC7650, 640 × 512 pixels, resolution = 14.15 μm/pixel), respectively. For our pulsed jet cooling studies, the IR camera was configured for pixel binning, facilitating IR recordings at 870 frames per second (integration time: 0.435 ms, binned window size: 160 × 128 pixels, binned resolution = 56.6 μm/pixel). As shown in both Fig. 1 and Fig. 3(c), the testing sample is orientated in the jet or spray chamber with the "back-side" surface of the IR transparent glass substrate facing toward the IR camera and the "front-side" surface coated with the Ti heater or thermometer facing the impinging jet. As shown in Fig. 1, the high-speed visible camera is orientated for side viewing through a chamber port window. The thin-film Ti heater or thermometer is 99% opaque in thermal camera's sensitivity region, facilitating transient pixel-by-pixel local temperature measurements (see the Supplemental Material [23] for the details).

To estimate the emissivity of the Ti thin film and the corresponding temperature measurement error via IR thermometry, validation experiments were conducted using the IR camera and a K-type thermocouple in contact with the surface of the Ti heater or thermometer. Fig. 3(a) provides the raw data from these experiments. To facilitate this temperature assessment process, emissive black paint was spray-coated on the Ti thin film. We note that after these experiments that the black paint was removed by toluene washing. The first test run corresponds to the open-triangle data in Fig. 3(a), indicating the transient increase in the black paint's surface temperature (starting from ≈30 °C) measured by both the thermocouple and the IR camera for a constant applied heat flux of $q'' = 20 \pm 0.6$ W/cm^2. Figure 3(b) is a schematic illustration of the "front-side" measurement configuration for this test, where the IR camera's image plane coincides with the paint-air interface. The recorded thermocouple temperature (T_{TC}) is the local contact temperature in the center of the sample, while the IR camera temperature (T_{IR}) is an area-average temperature around the thermocouple's probe tip (view area: ≈1 mm^2), using the default FLIR ResearchIR MAX software emissivity ($\epsilon = 1$)

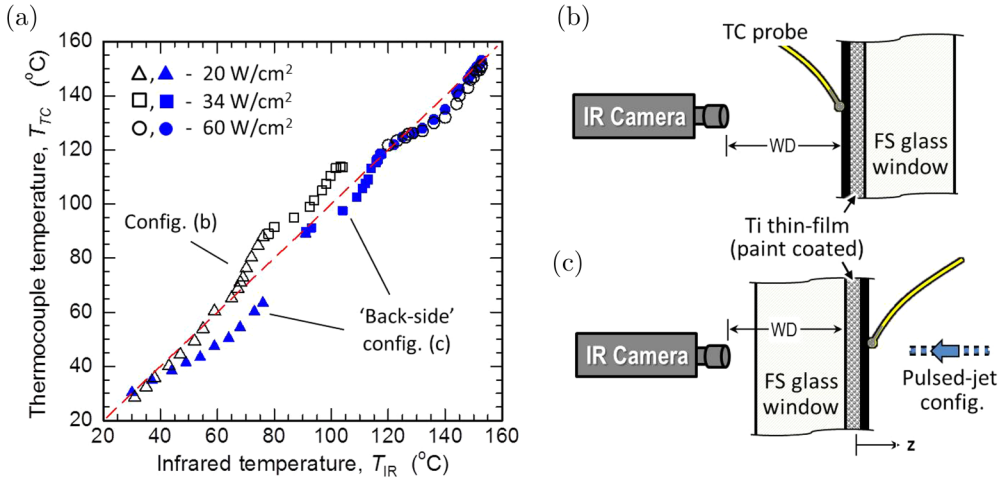

FIG. 3. (a) Comparison between the temperatures measured using IR (T_{IR}) and thermocouple (T_{TC}) thermometry. Data are provided for three different heat flux configurations and two different measurement configurations. The curvature in the data is due to transient heating effects (i.e., steady-state conditions are only applicable at $T_{IR} \approx 90$, 120, and 153 °C. (b) Schematic depiction of the "front-side" measurement configuration (not to scale). The open-symbol data in (a) were acquired for this "front-side" configuration. (c) Schematic depiction of the "back-side" measurement configuration (not to scale). This "back-side" schematic depicts an impinging jet; however, no jets were used during the data acquisition for the temperature data provided in (a). As illustrated in (b) and (c), the working distance (WD) was the same for both measurement configurations. Also, the emissive black paint coating on the Ti heater or thermometer was removed after these temperature cycling experiments.

for the black paint. The second test run is indicated by the open-square data in Fig. 3(a); thus, the same measurement configuration as the first test (open triangles) but at a higher applied heat flux of $q'' \approx 34\,\mathrm{W/cm^2}$. After data acquisition from this second test (open squares), the sample stage was allowed to heat to a steady-state temperature of ≈120 °C (via $q'' \approx 34\,\mathrm{W/cm^2}$). Then the heat flux was increased to the constant value of $q'' \approx 60\,\mathrm{W/cm^2}$ (open-circle data). Thus, the open-circle data in Fig. 3(a) show the temporal evolution of T_{IR} and T_{TC} (starting at ≈120 °C). For the subsequent tests (filled-symbol data), first the sample stage was cooled to room temperature (via ambient convection and conduction) and then rotated for "back-side" measurements. This back-side configuration depicted in Fig. 3(c) is the same configuration used for the pulsed jet experiments (i.e., IR imaging through the glass substrate with an imaging plane at the Ti-glass interface). For these back-side tests the IR emissivity setting was changed to $\epsilon = 0.45$ for Ti, yet the thermocouple tip was still in contact with the black paint on the Ti thin film (heater or thermometer). As shown in Fig. 3(a), $T_{TC} \leqslant T_{IR}$ holds for nearly all data (other than the first two "front-side" tests up to ≈110 °C). We attribute this temporal lag in T_{TC} relative to T_{IR} to imperfect thermocouple contact. The anomalous results for the first two "front-side" trials are attributed to temperature annealing of the emmissivity of the black paint coating. In support, the relative deviation between T_{IR} and T_{TC} is at most ≈3 °C at steady-state temperatures (i.e., at ≈30, 90, 120, and 150 °C). Yet, because our jet cooling studies are spatiotemporal in nature with T_{IR} of the Ti-glass interface varying spatially from ≈40 to ≈150 °C, we use the average temperature error observed for each applied heat flux in the pulsed jet ("back-side") experimental configuration. From this data in Fig. 3(a), we estimate a IR temperature accuracy of $\delta T_{IR} \approx \pm 6.6$, ± 4.5, and ± 4.2 °C for $q'' \approx 20$, 34, and 60 $\mathrm{W/cm^2}$, respectively. These temperature error estimates are accounted for in all subsequent heat transfer analysis.

D. Methodology and experimental conditions

The procedure for pulsed jet cooling experiments require several initiation steps, including flow-loop leakage inspection, flow-line evacuation testing, and water charging through the flow-loop. After flow-loop inspections, the open-line configuration was tested using the syringe needle and chopper wheel for pulsed jet cooling studies. For all jet cooling experiments, the distance between the heater surface and syringe needle outlet was kept constant at $H = 80$ mm. This work used three different jet pulsation set-point frequencies with corresponding Strouhal numbers ($\mathrm{St} = f_p D_{\mathrm{jet}}/U_{\mathrm{flow}}$) ranging from 0.002 to 0.0045 at a constant Reynolds number ($\mathrm{Re} = \rho_w U_{\mathrm{flow}}/\mu_w$) of $\mathrm{Re} \approx 970$. The jet pulsation frequency, f_p is defined as the number of jet on-off cycles per second. These on-off states of the jet were controlled by physically chopping a steady jet stream using a custom Al mechanical chopper wheel attached to the shaft of a dc motor (see the Supplemental Material [23] for the details).

The wall heat flux was generated by joule heating the Ti thin film using the voltage-current monitoring power supply operated in a dc mode. All experiments were performed at ambient conditions ($T_{\mathrm{amb}} \approx$ 22.5 °C and $RH \approx 60\%$). The transient local heat flux generated by the Ti thin-film heater or thermometer takes into account the conductive losses into the FS glass substrate via

$$q''(x, y, t) = \frac{I^2 R_{\mathrm{Ti}}}{A} - \left[\frac{T_s(x, y, t) - T_z}{\Delta}\right] k_{\mathrm{FS}}, \tag{1}$$

where k_{FS} is the thermal conductivity of the FS substrate, I is the applied current, R_{Ti} is the temperature-dependent electrical resistance of the Ti thin film, and A is the surface area of the Ti thin film.

The IR camera is aligned and focused on the Ti surface, where the surface roughness and imperfections in the Ti thin film allow for easy alignment. The thermal camera directly measures the Ti surface-interface temperature because the Ti thin film is opaque in the IR region (please see the Supplemental Material [23] for the details). The thickness of the Ti heater or thermometer is very thin (≈100 nm). Therefore, the conduction resistances (normal to the plane) in the Ti are negligible compared to the convective resistance and 1D conduction corrections are not necessary [24]. Moreover, thermal inertia is neglected because the Ti thin film is only ≈100 nm thick (see the Supplemental Material [23] for details). Pixel-by-pixel IR thermal imaging data are recorded for steady-state wall heat flux conditions using the ResearchIR MAX software, where a Python code handles (i) pixel-by-pixel temperature ($T_s(x, y, t)$), (ii) fluid temperature (T_f), and (iii) the local heat flux ($q''(x, y, t)$). Thus, pixel-by-pixel heat transfer coefficients are generated at different heat flux and pulsed jet impingement conditions. The heat transfer coefficient in this subcooled jet impingement cooling regime can be simply calculated with

$$h(x, y, t) = \frac{q''(x, y, t)}{T_s(x, y, t) - T_f}. \tag{2}$$

E. Uncertainty analysis

Heat flux errors were found to be in the range of ±3% (see the Supplemental Material [23] for the details). As discussed in Sec. II C, the accuracy of our IR temperature measurements are estimated to be within $\delta T_{\mathrm{IR}} \approx 4.2$–$6.6$ °C. The influence of the working distance of the IR camera on accuracy of temperature measurements is also discussed in Supplemental Material [23]. Although not necessary, Gaussian filters are employed in the Python code to get smooth thermal and heat transfer coefficient (HTC) contours (see the Supplemental Material [23] for the details). The corresponding error in our HTC measurements are expected to range within 25 to 28% due to our large δT_{IR} estimates. All error bars in the subsequent data are based on these uncertainty estimates.

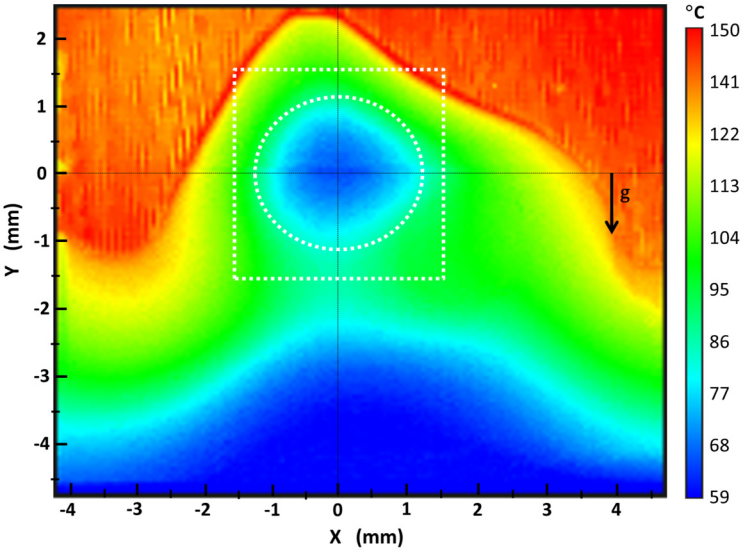

FIG. 4. Infrared (IR) temperature map for pulsed jet cooling. The image dimensions are centered to the jet stagnation point [$(X, Y) = (0, 0)$ mm]. The circle and square overlays correspond to the jet impingement zone (JIZ) and radial-flow zone (RFZ) for subsequent analysis (areas: $A_{\mathrm{JIZ}} \approx 4.2$ mm^2, $A_{\mathrm{RFZ}} \approx 9.7$ mm^2). Experimental details: $t \approx 0.936$ s (relative to the start of IR data acquisition), $q'' = 60 \pm 2$ W/cm^2, $f_p = 14.95 \pm 0.97$ Hz, $G \approx 795$ kg/m^{2}s, Re ≈ 970, St ≈ 0.003, $D \approx 410$ μm, $H/D \approx 200$, and $z > 0$ into the page or image.

III. RESULTS AND DISCUSSION

A. Spatiotemporal HTC characterization for pulsed jet cooling

Figure 4 shows a typical infrared temperature map acquired during a pulsed jet impingement experiment. The data in Fig. 4 are for an applied heat flux of $q'' \approx 60$ W/cm^2 and a jet pulsation frequency of $f_p \approx 15$ Hz. The spatiotemporal nature of this pulsed jet cooling process is further depicted in Fig. 5. Figure 5(a) provides the area-averaged, temporal response for both the measured Ti thin-film temperature (left axis) and the calculated HTC (right axis) within the jet impingement zone (JIZ). We point out that the area-averaged Ti interface-wall temperature fluctuates at the expected timescale for pulsed jet cooling (i.e., $\delta t \approx 1/f_p$). Figure 5(b) highlights the spatial distribution of the wall temperature (left axis) and HTC (right axis) across the jet stagnation point within the radial-flow zone (RFZ). The zoomed-view temperature maps in Figs. 5(c) and 5(d) also provide the corresponding HTC distributions calculated via Eq. (2), where $T_s = T_I^*$ is the Ti thin-film interface-wall temperature. As expected, the minimum wall temperatures are observed at the jet stagnation point [i.e., at $[X, Y] = [0, 0]$ mm in Figs. 5(c) and 5(d)]. Supplemental Material [23] provide analogous surface temperature and HTC mapping data for all the pulsed jet cooling configurations studied in this work. Supplemental video 1 provides the corresponding IR video acquired for Figs. 4 and 5 ($q'' = 60 \pm 2$ W/cm^2, $f_p = 14.95 \pm 0.97$ Hz).

The pulsating nature of the jet induces slight oscillations in the calculated, area-averaged HTC values. These HTC (and surface temperature) oscillations are repeatable with an oscillation frequency matching the jet pulsation frequency. For example, with respect to the "jet impingement zone" data [Fig. 5(a)], the HTC increases from $\approx$10.85 kW/m^{2}K to $\approx$10.97 kW/m^{2}K within $\approx$15 ms after initiation of the "jet-on" state (or jet-cooling state). Then, this average "jet zone" HTC commonly has a plateau for $\approx$10–15 ms, followed by a further increase in $\approx$5–10 ms to the local peak HTC value of $\approx$11.04 kW/m^{2}K. However, during the "jet-off" state (or wall-heating state) the HTC decreases from $\approx$11.04 kW/m^{2}K to $\approx$10.85 kW/m^{2}K within $\approx$15–20 ms. The

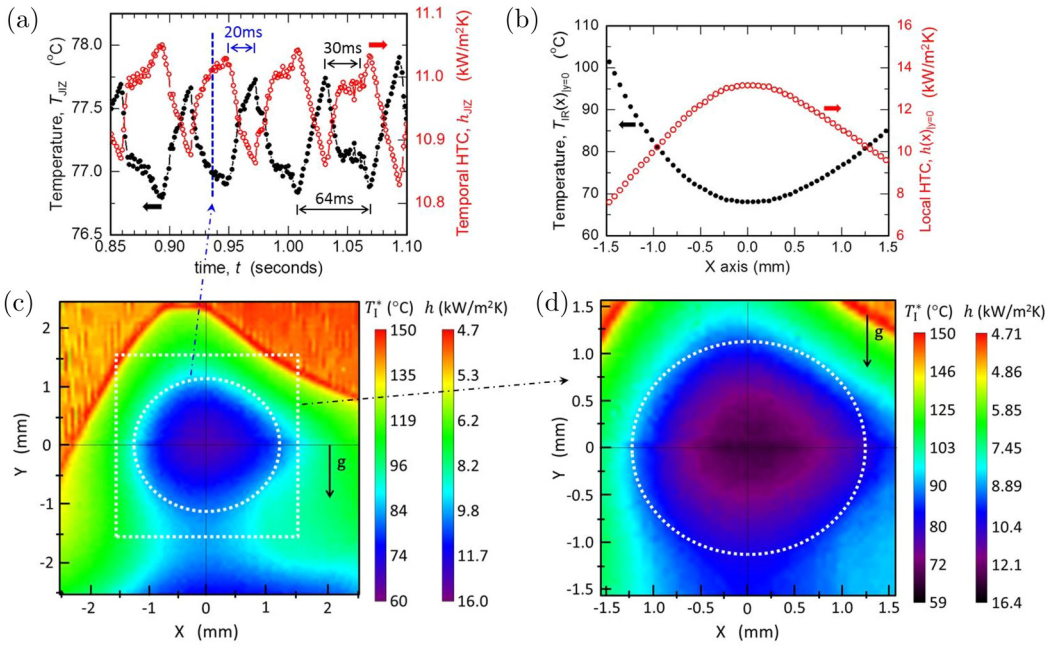

FIG. 5. Overview of key spatiotemporal temperature and HTC data for pulsed jet cooling using IR thermography. (a) Temporal Ti thin-film (wall-interface) temperature (left axis) and HTC (right axis). The data correspond to area-averaged values within the JIZ. (b) Spatial temperature (left axis) and HTC (right axis) profiles across the jet stagnation point [$(X, Y) = (0, 0)$ mm]. (c) The IR temperature map and corresponding HTC distribution at $t \approx 0.936$ s. (d) Zoom view of the RFZ and corresponding JIZ within it. Experimental details: $t \approx 0.936$ s (relative to the start of IR data acquisition), $q'' = 60 \pm 2$ W/cm^2, $f_p = 14.95 \pm 0.97$ Hz, $T_{\text{jet}} \approx 22.5\,^{\circ}$C, $D_{\text{jet}} \approx 410\ \mu$m, $G \approx 795$ kg/m^{2}s, Re ≈ 970, St ≈ 0.003, $H/D \approx 200$, and $z > 0$ into the page or images.

temporal timescales are nearly identical for local, maximum HTC data at the stagnation point (or a reduced area around the stagnation point—please see the Supplemental Material [23] for the details). However, the magnitude of these HTC (or wall temperature) oscillations are amplified at the stagnation point. Correspondingly, maximum heat transfer coefficients (or minimum surface temperatures) are observed at the center of JIZ. This is a universal trend observed for all f_p and q'' configurations studied in this work.

While the area-averaged temperature and HTC results are temporally consistent with the jet pulsation frequency (f_p), the corresponding IR temperature maps (i.e., IR image snapshots) are not spatially uniform. The asymmetric nature in the temperature profile is due to the falling-film behavior of the fluid flow field. This is clearly illustrated all the IR imagery data. In addition, the IR imagery data in Figs. 5(c) and 5(d) show that the HTC (or surface temperature) contours within the jet impingement zone keep rather parallel to each other, signifying uniform thermal diffusion within the jet impingement zone. However, at larger length scales (e.g., outside the jet impingement zone) the HTC maps are distorted, especially at the bottom of the radial-flow zone due to falling-film cooling effects. Supplemental Material [23] provides additional data of the spatial HTC and wall temperature distributions around the stagnation point.

Figure 6 provides an overview of the HTC measured as a function of the jet pulsation frequency (f_p) for the different heat flux configurations studied in this work. The enhancement of the heat transfer coefficient with increasing pulsation frequency is potentially due to interfacial waves and boiling events. We note that no boiling events were observed for $q'' = 20 \pm 2$ W/cm^2. Interfacial

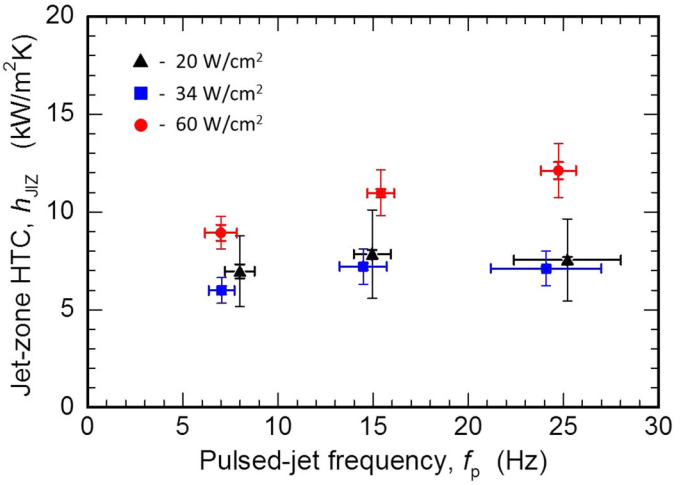

FIG. 6. HTC data as a function of jet pulsation frequency and applied heat flux. The HTC values are based on area-averaged wall-interface temperatures within the JIZ. The relative error in f_p is based on temporal analysis of the acquired T_{JIZ} data, where T_{JIZ} is the average spatiotemporal wall temperature recorded within the jet impingement zone during an IR acquisition period of ≈5 s (see Supplemental video 1). The relative error in h_{JIZ} is provided based error propagation using the standard deviation in the applied heat flux ($\delta q''$) combined with either (i) δT_{IR} ("larger error-bar data") estimated from the temperature cycling studies (Sec. II C) or (ii) δT_{JIZ} ("smaller error-bar data") due to temporal drift in T_{JIZ} measured throughout an entire ≈5-s IR data acquisition. Experimental details: $T_{jet} \approx 22.5\,^{\circ}$C, $D_{jet} \approx 410\ \mu$m, $G \approx 795$ kg/m^{2}s, Re ≈ 970, St ≈ 0.003, $H/D \approx 200$, $q'' = 20 \pm 0.6$, 34 ± 1, and 60 ± 1.8 W/cm^2, $f_p = 7.99 \pm 0.77$, 14.95 ± 0.97, and 25.21 ± 2.81 Hz.

waves increase the effective interfacial area causing the mean film thickness to drop at the radial locations from the stagnation point of the impinging jet. Moreover, boiling events appear between radial-flow waves that are observed at the highest heat flux condition studied ($q'' \approx 60$ W/cm^2). This potentially reduces the overall thermal resistance at the edge of the jet impingement zone. For such heat and mass transfer conditions, the overall heat transfer performance is enhanced [52]. Further discussion on these HTC data is provided in Sec. III D with reference to our theoretical predictions and the maximum HTC values observed at the jet's stagnation point.

B. Pulsed jet boiling events

Figure 7 illustrates the cyclic events that occur during pulsed jet impingement cooling for a heat flux condition of $q'' \approx 60$ W/cm^2). Bubble nucleation is clearly visible at different locations on the Ti heater or thermometer surface—especially near the edge of the jet impingement zone. Figure 7(a) shows bubble nucleation at $t \approx 92$ ms. The subsequent images [i.e., Figs. 7(b), 7(c), and 7(d)] show that within ≈18 ms the vapor bubbles have completely collapsed to a millimeter-sized dry-out region. In fact, the vapor bubbles collapse in ≈1–2 ms. For example, Fig. 7(b) shows the fully developed dry-out region at $t \approx 114$ ms. Moreover, after a complete dry-out event [7(a)→ 7(b)], the heater surface is partially rewetted [7(c)]. Then, a full rewetting of the surrounding water jet or droplets occurs [7(d)]. This development of a fully rewetted zone occurs via a coexistence of both a thin-film fluid layer and a newly impinging jet. The occurrence of these cyclic boiling, dry-out, and rewetting events was observed to be very random; however, the corresponding time duration of each event tended to be rather universal. As previously illustrated in the spatiotemporal IR data in Fig. 5, these major cyclic events occur on the heater surface with highly radial thermal gradients and at relatively low local wall subcooling temperatures. Thus, the maximum HTCs are observed at the

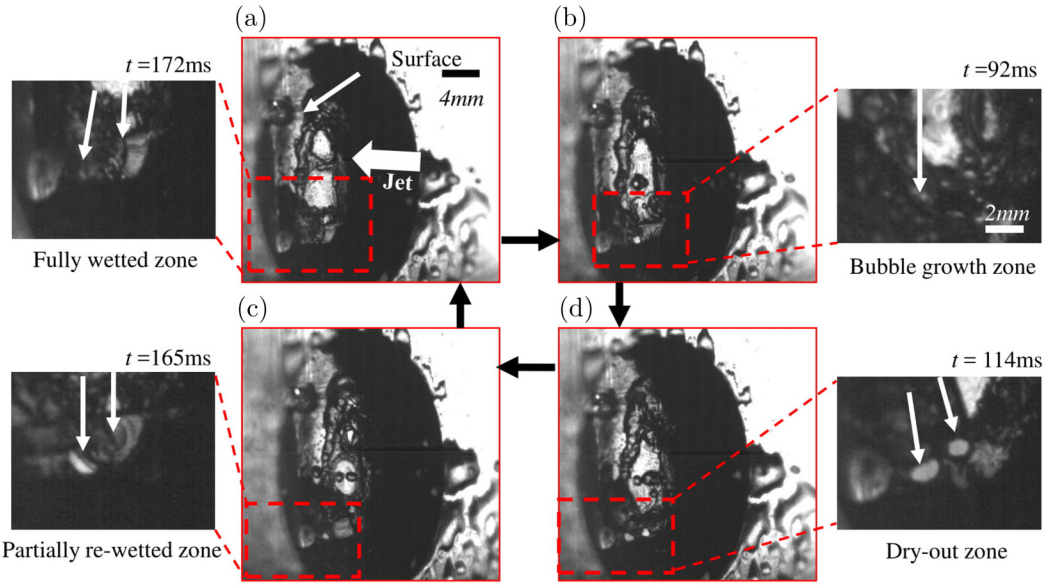

FIG. 7. High-speed visible imagery data for the jet impingement and falling thin-film boiling cycles ($f_p \approx$ 15 Hz, $q'' \approx 60$ W/cm^2, $G \approx 795$ kg/m^2 s, Re ≈ 970). (a) Image of bubbles starting to appear at a radial location from center of the impinging jet. (b) Visual representation of dry-out zones as the bubbles tend to grow and collapse. (c) Image showing that the surrounding water coolant tends to wet the dry-out zones with the appearance of partially rewetted zones. (d) Imagery of the fully wetted zones as the next jet or droplet pulse of liquid starts to impact the heated wall.

center of the jet impingement zone. A potential mechanism for these cyclic boiling events during pulsed jet cooling is further discussed in Supplemental Material [23].

C. Falling film instability criterion

To further investigate the role of the pulsed jet in terms of a critical pulsation frequency, the instability associated with falling liquid film under gravity must be understood. This falling liquid film encounters interfacial instabilities because of pressure difference at the liquid-air interface [53]. These instabilities caused by a pulsating jet are mainly due to the imbalance in the inertia and thermocapillary forces (due to surface tension gradients in the liquid film and tangential shear stress at the solid-liquid interface) [54–57]. The dominance of the inertia force due to the unsteady (pulsating) nature of the jet can be described by Strouhal number [58]. These instabilities are fueled by thermocapillary breakdown when a pulsed liquid jet comes into contact with heated surface (please see the Supplemental Material [23] for the details). During this modulated (unsteady) two-phase cooling process, the boiling events at radial locations of the impinging jet appear in cycles. The oscillating nature provides rigorous vapor formation at high thermal loads. Such pulsed perturbations assist the formation of an unsteady vapor blanket that exerts a tangential shear stress on the radially flowing and oscillating liquid thin film. The change in the film thickness from the wave crest to the wave trough causes potentially additional perturbations in gravity-induced flow rate. Moreover, the tangential stress opposes this gravity effect and subsequently decreases the overall flow-rate perturbations within the liquid-film region. Thus, the tangential stresses reduce the inertia-driven radial flow rate, which further suppresses the Kapitza instability [59,60].

An empirical correlation is beneficial to predict critical Marangoni number for wide range of Reynolds numbers [48]. The following relation can be used to correlate the Maragoni (Ma), Prandtl

(Pr), and Re numbers for a falling liquid film:

$$\frac{\mathrm{Ma}}{\mathrm{Pr}} = 0.115\mathrm{Re}^{0.65}, \tag{3}$$

where $\mathrm{Ma} = \partial\gamma/\partial T \times \delta\Delta T/\mu\alpha$, $\mathrm{Pr} = \nu/\alpha$, γ is the surface tension, δ is film thickness, and $\alpha = k/\rho c_p$ and $\nu = \mu/\rho$ are the thermal and momentum diffusivity, respectively. During boundary layer formation, the falling film velocity is similar to that of the jet impingement velocity. Thus, the falling film is not influenced by the heater's surface roughness but is influenced by the gravitational body force. And, for a gravity-induced falling film, asymmetric large waves (preceded by small ripples) form due to Kapitza instability [60].

The critical wavelength of the ripples in this falling film can be described via the Rayleigh-Taylor instability wavelength [61]:

$$\lambda_o = 2\pi\sqrt{\frac{\gamma}{g(\rho_l - \rho_a)}}, \tag{4}$$

where ρ_l and ρ_a are density of liquid and air, respectively.

Lel *et al.* [25] modeled the thermocapillary breakdown of these larger waves (i.e., waves with $\lambda \gg \lambda_o$) due to perturbation of liquid film on a heated surface. This work yielded an instability criterion in terms of a nondimensional Kapitza number (Ka). Neglecting the friction at the water-air interface, the instability criterion can be expressed as

$$\frac{\mathrm{Ma}}{\mathrm{PrKa}} = 0.093\frac{U_r}{U_w}, \tag{5}$$

where $\mathrm{Ka} = (f_w\lambda_o/\nu^{1/3}g^{1/3})^2$. Moreover, U_r, U_w, f_w signify residual layer velocity, wave velocity and perturbation frequency, respectively. Ambrosini *et al.* [62] provided an experimental evidence for heated water as to how these wave velocity (U_w) and residual layer velocity (U_r) can be scaled with Reynolds numbers (please refer to Fig. 14 of their article). From their investigation, the ratio of wave velocity to residual layer velocity is found to be between 2 and 2.2 for warm water (70 °C). Thus, Eqs. (3)–(5) can be used to predict a dominant (or critical) perturbation frequency for heat and mass transfer in a falling liquid film. During our pulsed jet cooling experiments, this perturbation is induced by the impact of the pulsed jet on the heated substrate. Therefore, the dominant perturbation frequency, $f_{\mathrm{Ka}} = (\mathrm{Ka}\nu^{1/3}g^{1/3}/\lambda_o)^{0.5}$ can be potentially used to determine the optimum pulsation frequency, f_p (please see the Supplemental Material [23] for the details). We note that for this study that $\mathrm{Re} \approx 970$ and the mass flux was fixed at $G \approx 795$ kg/m^{2}s. Nevertheless, a critical jet pulsation frequency [via Eqs. (3)–(5)] of $f_p = f_{\mathrm{Ka}} \approx 18.9$–$19.8$ Hz is expected in this work. As a result, we initially anticipated to observe a roll-off (decrease) in the thermal cooling performance for pulsed jets with $f_p > f_{\mathrm{Ka}}$. However, no clear connection between f_p and f_{Ka} is observed for augmenting the overall heat transfer performance (see Fig. 7 and subsequent discussion).

It is important to note that the absence of the Ka in Eq. (3) makes it difficult to directly couple Eq. (5) with Eq. (3). Ideally, a predictive correlation for thermocapillary breakdown in the falling-film configuration should be dictated by the Re, Pr, Ma, Ka, and Boiling number (Bg). The boiling number is important during multiphase cooling because interfacial heat transfer depends on both the local heat flux and vapor quality. To produce a more robust and compatible empirical or semiempirical model, more experiments are needed with a broad range of heat fluxes and working fluids. This would also lead to better predictions of the cut-off frequency.

D. Instantaneous heat flux matching

To further understand the influence of the jet pulsation frequency on the cooling performance (i.e., the HTC) we must first acknowledge that this cooling process is dictated by several thermofluid transients. We note that for all transient thermal transport processes that the heat flux must be matched at the interface between two dissimilar materials (e.g., at the FS-Ti and Ti-jet interfaces).

A transient heat source is commonly described in terms of its thermal penetration depth (l_{th}). The thermal penetration depth for a modulated heat source can be given by $l_{\text{th}} = \sqrt{2\alpha/\omega}$, where $\omega = 2\pi f_p$ is the angular modulation frequency of the heat source. An impinging jet on a heated surface also leads to either a fully developed or developing thermal boundary layer (depending on the transient nature of thermofluid dynamics). The average thickness of the thermal boundary layer (for both steady and unsteady conditions) can be expressed as $\delta_{\text{th}} = k/h_\omega$, where k is the thermal conductivity of the fluid and h_ω is the frequency dependent heat transfer coefficient [47]. This transient HTC is dictated by both the thermal effusivity of the fluid and the transient timescales of the thermal transport process, i.e., $h_\omega \propto e_{\text{th}}\sqrt{\omega}$, where for steady-state conditions either (i) $\omega \to 0$ or (ii) $\omega \to \infty$. The latter applies to only ultra-high-frequency situations when the magnitude of the perturbation amplitudes are negligible. In regards to the former, we note that $h_{\omega\to 0}$ is the traditionally reported HTC for macroscale thermal transport [47]. Thus, for transient heat and mass transfer in a thin liquid film, δ_{th} can be of the same order as l_{th} for relatively low-frequency temperature (or flow-field) oscillations. For example, $l_{\text{th}} \gtrsim \delta_{\text{th}}$ when $f_p \lesssim 50$ Hz—based on typical thermofluid characteristics of a water cooling process ($k = 0.6$ W/m K, $\alpha = 0.15 \times 10^{-6}$ m^2/s, $h \approx 20$ kW/m^2 K). Nevertheless, the transient thermal boundary layer thickness scales with the thermal penetration depth as $l_{\text{th}} = \sqrt{2}\delta_{\text{th}}$, which leads to the following:

$$\frac{k_{\text{jet}}}{h_{\max}} = \sqrt{\frac{\alpha_{\text{jet}}}{2\pi f_p}}. \tag{6}$$

Rewritting Eq. (6) in terms of the thermofluid perturbation frequency leads to the following relation for a critical frequency at a solid-liquid interface:

$$f_p^* = \left(\frac{h_{\max}}{\epsilon_{\text{th}}}\right)^2 \frac{1}{2\pi}, \tag{7}$$

where $e_{\text{th}} = \sqrt{k\rho c}$ is thermal effusivity of the working fluid. Assuming that the contact resistance between solid heater wall and liquid jet is negligible, the solid-liquid interface temperature (T_{I^*}) must be constant (temporally invariant) for timescales less than that required for steady heat transport (i.e., T_{I^*} is a constant for $t \leqslant 1/f_p^*$).

Although the temperature profile inside the two bodies in contact will be evolving in time, during this transient pulsed jet cooling process the instantaneous heat flux across the wall interface must be continuous (i.e., a balance between solid-to-wall and wall-to-jet heat flux $-q''_{s\to \text{Ti}} = q''_{\text{Ti}\to\text{jet}}$). This requirement for instantaneous heat flux matching yields a unique wall-interface temperature,

$$T_{I^*} = \frac{T_s e_{\text{th},s} + T_{\text{jet}} e_{\text{th,jet}}}{e_{\text{th},s} + e_{\text{th,jet}}}, \tag{8}$$

where $e_{\text{th},s}$ and $e_{\text{th,jet}}$ are the thermal effusivities of the solid FS substrate and pulsed water jet (respectively) and T_s and T_{jet} are the steady-state substrate and jet temperatures outside the thermal boundary layer ($|z| > \delta_{\text{th}}$) [63]. However, because the pulsed jet induces spatiotemporal convection heat transfer from the heater wall-interface, an effective thermal effusivity of the pulsed jet should be used to accurately represent the experimentally observed thermal response at the wall-jet interface. In this regard, Eq. (8) can be rewritten as

$$e_{\text{th,jet}}^{\text{eff}} = \epsilon_{\text{th},s} \frac{T_s - T_{I^*}}{T_{I^*} - T_{\text{jet}}}, \tag{9}$$

where now the unique wall-jet interface temperature (T_{I^*}) is directly correlated to the measured Ti heater or thermometer surface temperature (i.e., $T_{I^*} \approx T_{\text{Ti}}$ via measurement by IR thermometry).

For jet impingement cooling with a steady laminar jet, the local heat transfer coefficient is of the form: $h_0 = (k/L_c)\text{Nu}$, where L_c is a critical length scale for this forced convection cooling process and the Nusselt number can be expressed as $\text{Nu} = 0.332\text{Pr}^{1/3}\text{Re}^{1/2}$. We note that Nu is commonly expressed with coefficients >0.332 and different powers for Pr and Re [64,65]; however, to (i)

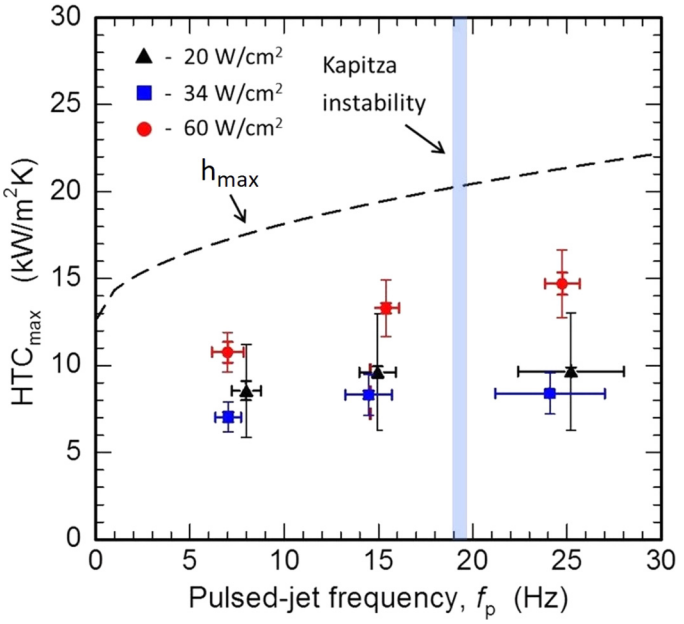

FIG. 8. Impact of the jet pulsation frequency on the maximum heat transfer coefficient measured (symbols) and predicted (dashed lines) in this work. The HTC values correspond to the maximum values measured at the jet stagnation point. The error bars for the HTC data are derived based on the same methodology addressed in Fig. 6. The predicted HTC is based on h_{max}: Eq. (10). The vertical dashed line is predicted frequency for Kapitza instability criterion [f_{Ka} via Eqs. (3)–(5)].

avoid data fitting and (ii) conserve first-principle derivations thereof, we use 0.332, $Pr^{1/3}$, and $Re^{1/2}$. Notwithstanding the functional form for this steady, dimensionless HTC (Nu), the heat transfer coefficient for pulsed jet cooling can be now predicted by augmenting the "steady laminar jet" HTC with that from Eqs. (7)–(9); i.e., $h = h_0 + h_\omega$. The maximum heat transfer coefficient expected for pulsed jet cooling is

$$h_{\max} = 0.332\frac{k_{\text{jet}}}{\sqrt{2}D_{\text{jet}}}\text{Pr}^{1/3}\text{Re}^{1/2} + e_{\text{th}}^{\text{eff}}\sqrt{\frac{2f_p}{\pi}}, \tag{10}$$

where $L_c = \sqrt{2}D_{\text{jet}}$ to account for expansion, $k_{\text{jet}} = k_{\text{water}} = 0.6$ W/mK, and $e_{\text{th,jet}}^{\text{eff}} = 2.2 \pm 0.3$ $\text{kWs}^{1/2}/\text{m}^2\text{K}$ is that calculated via Eq. (9) using $e_{\text{th},s} = 1.48$ $\text{kWs}^{1/2}/\text{m}^2\text{K}$ for FS and T_I^* measured in this work. For reference, the steady jet contribution to the HTC [first-term, Eq. (10)] is $h_0 \approx 12.6$ $\text{kW/m}^2\text{K}$. We also note that the $1/\sqrt{\pi}$ factor in the pulsed jet HTC contribution [second term, Eq. (10), in comparison to that obtained via rewritting Eq. (7)] is based on derivation using Newton's law of cooling, the finite superposition solution for $T(z,t)$ [63], and comparative analysis of the analytic solution for the wall heat flux (i.e., $-k\partial T(z,t)/\partial z$ evaluated at the wall ($z = 0$) and at a timescale of $t = 1/f_p$).

Figure 8 compares our predicted and measured HTCs for subcooled pulsed jet cooling in a falling liquid-film configuration. Both the measured and predicted data represent the local HTC values at the jet stagnation point. We note that maximum HTCs (or minimum surface temperatures) are observed at the jet stagnation point; e.g., at $(X, Y) = (0, 0)$ mm in Figs. 4 and 5. As illustrated in Fig. 8 fair agreement is observed between the experimental data and the theoretical predictions of heat transfer coefficient. The use of other correlations for the steady laminar jet contribution [64] yield comparable values for h_0 (i.e., $h_0 \approx$ 2–20 $\text{kW/m}^2\text{K}$); yet, those correlations were not

validated for the $H/D \approx 200$ used in this work. Also, our predictions based on instantaneous heat flux matching did not account for the temperature discontinuity at the liquid-vapor interfaces and flow-field instabilities. Therefore, if the estimates of e_{th}^{eff} do not indirectly account for such effects, then the theoretical model should be an overestimate the heat transfer coefficient. As discussed previously, for a jet pulsation frequency greater than the critical pulsation frequency (f_p^*), these instabilities are well suppressed which reduces the rate of enhancement in heat transfer coefficient. With this said, HTC suppression is not evident in our experimental data set. A better correlation between experiment and theory is expected given derivation of an analytic solution that can also account for the frequency dependence of the amplitude of the surface temperature oscillations. The magnitude of such surface-wall temperature oscillations [Fig. 5(a)] were observed to scale directly with the applied heat flux and indirectly with pulsed jet frequency. Also provided in Fig. 8 is the predicted Kapitza instability cut-off frequency [via Eqs. (3)–(5)]. For reference, the impact of the jet Reynolds number on this predicted cut-off frequency (f_{Ka}) is illustrated in Supplemental Material [23]. A roll-off (or plateauing) in the measured HTC was expected for jet pulsation frequencies $\gg f_{\text{Ka}}$ because a high-frequency pulsed jet will represent a turbulent jet. Moreover, at large heat fluxes and $f_p \gg f_{\text{Ka}}$ the spatiotemporal surface temperature fluctuations will be driven by chaotic boiling events. However, the current data set does not show any augmentation to the HTC other than the predicted $\sqrt{2f_p/\pi}$ dependence.

IV. CONCLUSION

Infrared thermography is shown to be a useful technique for mapping and visualizing spatiotemporal surface temperature (T_S) and HTC during pulsed jet impingement cooling on Ti-coated glass window. This investigation uses such data to understand two-phase thermofluid transients at the solid-liquid interface using the cooling rate and flow-field perturbations from pulsed jets. This work illustrates the important interdependence between the spatiotemporal cooling performance (i.e., the transient HTC distribution) and jet pulsation frequency. This interdependence was reinforced via analysis based on an instantaneous heat flux matching at the heat-source and heat-sink interface (glass-Ti and Ti-jet interfaces, respectively). Experimentally we observe that the HTC in the jet impingement zone increase in magnitude by ≈13–17% by increasing the jet pulsation frequency from ≈7 to ≈25 Hz. Moreover, using *in situ* high-speed visible videography, we captured the conjugate and cyclic boiling dynamics in concert with the pulsed jet impingement process (e.g., visualizations of the cyclic bubble growth, bubble collapse, wall dry-out, partial rewetting, and then full rewetting process). We observed during this cyclic boiling process that the jet pulsation frequency matches well the frequency associated with bubble release and wall dry-out. In addition to these findings, our maximum HTC predictions match well with our jet pulsation experiments.

ACKNOWLEDGMENTS

This material is based on research partially sponsored by the U.S. Office of Naval Research under Grant No. N00014-15-1-2481 and the National Science Foundation under Grant No. 1653396. The views and conclusions contained herein are those of the authors and should not be interpreted as necessarily representing the official policies or endorsements, either expressed or implied, of U.S. Office of Naval Research, the National Science Foundation, or the U.S. Government. We thank Dr. Louis Chow and Dr. Huseyin Bostanci for the part of the experimental flow-loop and insightful discussion, respectively. We also thank Bobby Enders (iREP, FLIR) for technical insights regarding thermal imaging systems.

[1] M. Ebadian and C. Lin, A review of high-heat-flux heat removal technologies, J. Heat Transf. **133**, 110801 (2011).

[2] S. G. Kandlikar and A. V. Bapat, Evaluation of jet impingement, spray and microchannel chip cooling options for high heat flux removal, Heat Transfer Eng. **28**, 911 (2007).
[3] J. Kim, Spray cooling heat transfer: The state of the art, Int. J. Heat Fluid Flow **28**, 753 (2007).
[4] J. Kim, Review of nucleate pool boiling bubble heat transfer mechanisms, Int. J. Multiphase Flow **35**, 1067 (2009).
[5] P.-S. Lee and S. V. Garimella, Saturated flow boiling heat transfer and pressure drop in silicon microchannel arrays, Int. J. Heat Mass Transf. **51**, 789 (2008).
[6] K. Jambunathan, E. Lai, M. A. Moss, and B. L. Button, A review of heat transfer data for single circular jet impingement, Int. J. Heat Fluid Flow **13**, 106 (1992).
[7] D. H. Wolf, F. P. Incropera, and R. Viskanta, Jet impingement boiling, Adv. Heat Transf. **23**, 1 (1993).
[8] R. Nevins and H. Ball, Heat transfer between a flat plate and a pulsating impinging jet, in *Proceedings of the National Heat Transfer Conference*, Vol. 60 (American Society of Mechanical Engineers (ASME), New York, NY, 1961), pp. 510–516.
[9] H. M. Hofmann, D. L. Movileanu, M. Kind, and H. Martin, Influence of a pulsation on heat transfer and flow structure in submerged impinging jets, Int. J. Heat Mass Transf. **50**, 3638 (2007).
[10] M. Chaudhari, B. Puranik, and A. Agrawal, Heat transfer characteristics of synthetic jet impingement cooling, Int. J. Heat Mass Transf. **53**, 1057 (2010).
[11] Y. W. Lyu, J. Z. Zhang, X. C. Liu, and Y. Shan, Experimental investigation of impinging heat transfer of the pulsed chevron jet on a semicylindrical concave plate, J. Heat Transf. **141**, 032201 (2019).
[12] M. R. Zargarabadi, E. Rezaei, and B. Yousefi-Lafouraki, Numerical analysis of turbulent flow and heat transfer of sinusoidal pulsed jet impinging on an asymmetrical concave surface, Appl. Therm. Eng. **128**, 578 (2018).
[13] S. Ghadi, K. Esmailpour, S. Hosseinalipour, and A. Mujumdar, Experimental study of formation and development of coherent vortical structures in pulsed turbulent impinging jet, Exp. Therm. Fluid Sci. **74**, 382 (2016).
[14] C. M. Hsu, W. C. Jhan, and Y. Y. Chang, Flow and heat transfer characteristics of a pulsed jet impinging on a flat plate, Heat Mass Transf. **56**, 143 (2020).
[15] C. Tang, J.-Z. Zhang, Y.-W. Lyu, and X.-M. Tan, Convective heat transfer on a flat target surface impinged by pulsating jet with an additional transmission chamber, Heat Mass Transf. **56**, 183 (2020).
[16] K. Esmailpour, B. Bozorgmehr, S. M. Hosseinalipour, and A. S. Mujumdar, Entropy generation and second law analysis of pulsed impinging jet, Int. J. Numer. Methods Heat Fluid Flow **25**, 1089 (2015).
[17] H. Yadav, A. Agrawal, and A. Srivastava, Mixing and entrainment characteristics of a pulse jet, Int. J. Heat Fluid Flow **61**, 749 (2016).
[18] Z. Trávníček and T. Vít, Impingement heat/mass transfer to hybrid synthetic jets and other reversible pulsating jets, Int. J. Heat Mass Transf. **85**, 473 (2015).
[19] Y. Zhang, P. Li, and Y. Xie, Numerical investigation of heat transfer characteristics of impinging synthetic jets with different waveforms, Int. J. Heat Mass Transf. **125**, 1017 (2018).
[20] X. Xia and K. Mohseni, Transitional region of a round synthetic jet, Phys. Rev. Fluids **3**, 011901 (2018).
[21] S. Ghadi, K. Esmailpour, M. Hosseinalipour, and M. Kalantar, Dynamical study of pulsed impinging jet with time varying heat flux boundary condition, Heat Transf. Asian Res. **45**, 85 (2016).
[22] H. Bostanci, B. He, and L. C. Chow, Spray cooling with ammonium hydroxide, Int. J. Heat Mass Transf. **107**, 45 (2017).
[23] See Supplemental Material at http://link.aps.org/supplemental/10.1103/PhysRevFluids.5.094003 for further discussion on pulsed jet duty cycles, characterization, error propagation, accuracy of thermal reading, transient thermal or heat transfer maps, cyclic boiling events, thermocapillary breakdown, optimum pulsation frequency, and influence of the Reynolds number, which includes Refs. [4,9,10,24–51].
[24] N. S. Dhillon, J. Buongiorno, and K. K. Varanasi, Critical heat flux maxima during boiling crisis on textured surfaces, Nat. Commun. **6**, 8247 (2015).
[25] V. Lel, H. Stadler, A. Pavlenko, and R. Kneer, Evolution of metastable quasi-regular structures in heated wavy liquid films, Heat Mass Transf. **43**, 1121 (2007).
[26] I. D. Mash and G. P. Motulevich, Optical constants and electronic characteristics of titanium, Sov. Phys. JETP **36**, (1973).

[27] Refractive index info, https://refractiveindex.info/?shelf=main&book=Ti&page=Mash.
[28] Thermoworks, https://www.thermoworks.com/emissivity-table.
[29] Researchir max by flir, https://www.flir.com/products/researchir/.
[30] Uncertainty in ir thermal recording, https://www.flir.com/discover/rd-science/infrared-camera-accuracy-and-uncertainty-in-plain-language/.
[31] F. P. Incropera, A. S. Lavine, T. L. Bergman, and D. P. DeWitt, *Fundamentals of Heat and Mass Transfer* (Wiley, New York, 2007).
[32] A. Tawfek, Heat transfer and pressure distributions of an impinging jet on a flat surface, Heat Mass Transf. **32**, 49 (1996).
[33] Y.-Y. Li, Y.-J. Chen, and Z.-H. Liu, Correlations for boiling heat transfer characteristics of high-velocity circular jet impingement on the nano-characteristic stagnation zone, Int. J. Heat Mass Transf. **72**, 177 (2014).
[34] W. Minkina and D. Klecha, Atmospheric transmission coefficient modeling in the infrared for thermovision measurements, J. Sens. Sens. Syst. **5**, 17 (2016).
[35] The ultimate infrared handbook by flir, https://vault.flir.com/file/asset/18320/original?token=8df9f33c-ebf4-43ce-897e-4fdeb4672a18.
[36] How far can i measure with a thermal camera accurately, https://www.controlengeurope.com/article/163635/How-far-can-I-measure-with-a-thermal-imaging-camera-.aspx.
[37] S. Bankoff, Entrapment of gas in the spreading of a liquid over a rough surface, AIChE J. **4**, 24 (1958).
[38] B. Mikic, W. Rohsenow, and P. Griffith, On bubble growth rates, Int. J. Heat Mass Transf. **13**, 657 (1970).
[39] P. Griffith and J. D. Wallis, *The Role of Surface Conditions in Nucleate Boiling*, Technical Report No. 14 (Massachusetts Institute of Technology Cambridge, MA, 1958).
[40] W. Fritz, Berechnung des maximalvolumes von dampfblasen, Physik Zeitschr **36**, 379 (1935).
[41] L. Maltsev, Y. S. Podzharov, and O. Kabov, Dry spot growth criterion for isothermal liquid films on a horizontal substrate, Thermophys. Aeromech. **24**, 383 (2017).
[42] F. F. Simon and Y.-Y. Hsu, *Thermocapillary Induced Breakdown of a Falling Liquid Film* (National Aeronautics and Space Administration, Washington, DC, 1970).
[43] V. G. Levich, *Physicochemical Hydrodynamics*, Vol. 115 (Prentice-Hall, Englewood Cliffs, NJ, 1962).
[44] Y. Y. Hsu, F. F. Simon, and J. F. Lad, Destruction of a thin liquid film flowing over a heating surface, Chemical Engineering Progress Symposium Series **57**, 139 (1965).
[45] E. A. Chinnov, Formation of the unsteady thermocapillary structures in the residual layer of three-dimensional waves, Int. J. Heat Mass Transf. **108**, 2053 (2017).
[46] S. H. Davis, Thermocapillary instabilities, Annu. Rev. Fluid Mech. **19**, 403 (1987).
[47] M. Mehrvand and S. A. Putnam, Transient and local two-phase heat transport at macro-scales to nano-scales, Commun. Phys. **1**, 21 (2018).
[48] D. V. Zaitsev, O. A. Kabov, V. V. Cheverda, and N. S. Bufetov, The effect of wave formation and wetting angle on the thermocapillary breakdown of a falling liquid film, High Temp. **42**, 450 (2004).
[49] J. H. Lienhard, Heat transfer by impingement of circular free-surface liquid jets, in *Proceedings of the 18th National and 7th ISHMT-ASME Heat and Mass Transfer Conference* (Tata McGraw-Hill, New Delhi, India, 2006).
[50] X. Gao, L. Kong, R. Li, and J. Han, Heat transfer of single drop impact on a film flow cooling a hot surface, Int. J. Heat Mass Transf. **108**, 1068 (2017).
[51] H. Leocadio, C. Van Der Geld, and J. C. Passos, Rewetting and boiling in jet impingement on high temperature steel surface, Phys. Fluids **30**, 122102 (2018).
[52] A. Pavlenko, A. Matsekh, N. Pecherkin, R. Kneer, V. Lel, and A. Surtaev, Heat transfer and crisis phenomena with intense boiling in the falling wave liquid films, Thermophys. Aeromech. **13**, 85 (2006).
[53] W. Meng, *A Study on Characteristics of a Thin Liquid Film Flowing down a Uniformly Heated Plate with Constant Heat Flux* (KTH, School of Science, 2018).
[54] D. Skamnakis and K. Papailiou, Flow stability analysis and excitation using pulsating jets, C. R. Mec. **333**, 628 (2005).
[55] H. Yadav and A. Agrawal, Effect of pulsation on the near flow field of a submerged water jet, Sādhanā **43**, 44 (2018).

[56] V. L. Okulov, I. V. Naumov, R. F. Mikkelsen, I. K. Kabardin, and J. N. Sørensen, A regular strouhal number for large-scale instability in the far wake of a rotor, J. Fluid Mech. **747**, 369 (2014).
[57] S. Leib and M. Goldstein, Convective and absolute instability of a viscous liquid jet, Phys. Fluids **29**, 952 (1986).
[58] V. Struhal, Uebereinebesondere art der tonerregung (on an unusual sort of sound excitation), Ann. Phys. Chem. **3**, 216 (1878).
[59] G. Lavalle, Y. Li, S. Mergui, N. Grenier, and G. F. Dietze, Suppression of the kapitza instability in confined falling liquid films, J. Fluid Mech. **860**, 608 (2019).
[60] G. F. Dietze, On the kapitza instability and the generation of capillary waves, J. Fluid Mech. **789**, 368 (2016).
[61] L. J. W. S. Rayleigh, *Investigation of the Character of the Equilibrium of an Incompressible Heavy Fluid of Variable Density* (Proceedings of the London Mathematical Society, London, 1883).
[62] W. Ambrosini, N. Forgione, and F. Oriolo, Statistical characteristics of a water film falling down a flat plate at different inclinations and temperatures, Int. J. Multiphase Flow **28**, 1521 (2002).
[63] E. R. G. Eckert and R. M. J. Drake, *Analysis of Heat and Mass Transfer* (Hemisphere Publishing, New York, 1972), pp. 165–166, 171–173.
[64] X. Liu, L. A. Gabour, and J. H. Lienhard V, Stagnation-point heat transfer during impingement of laminar liquid jets: Analysis including surface tension, ASME J. Heat Transf. **115**, 99 (1993).
[65] A. Bejan, *Convection Heat Transfer*, 4th ed. (John Wiley & Sons, Hoboken NJ, 2013), pp. 165–166, 171–173.